Investigations on the Electronic Excitations through Spectroscopic Measures for Resistive Switching Character of Manganite Thin Films

Kunalsinh N. Rathod, Keval Gadani, Davit Dhruv, Hetal Boricha, Alpa Zankat, Ashvini D. Joshi, Jitendra P. Singh, Keun H. Chae, Kandasami Asokan, Piyush S. Solanki, and Nikesh A. Shah*

Herein, an enhancement in the resistive switching of $Y_{0.95}Sr_{0.05}MnO_3$ (YSMO) films by swift heavy ion (SHI) irradiation-induced electronic excitations is shown. YSMO films are prepared by pulsed laser deposition on a single-crystalline Si substrate. For electronic excitations, Ag^{15+} ions with 200 MeV energy are used with ion fluences of 1×10^{11} (YS1), 1×10^{12} (YS2), and 1×10^{13} (YS3) ions per cm^2. X-ray diffraction shows increase in tensile strain up to YS2 film followed by strain relaxation in YS3 film. Red shifting of Raman active modes signifies the phonon softening due to tensile strain in pristine (YSP) to YS2 films. Atomic force micrographs show that the number and size of defects are increased, indicating the irradiation-induced defect formation, which is suppressed for the YS3 film. Rutherford backscattering spectrometry demonstrates decreased oxygen peak intensities for YS1 and YS2 films, denoting increased oxygen vacancies. Near-edge X-ray absorption fine structure displays a reduction in Mn valence state from Mn^{4+} to Mn^{3+}, signifying the formation of oxygen vacancies for films up to YS2. The enhancement of resistive switching is governed by tuning the SHI-induced oxygen vacancies. The present study demonstrates that YSMO films are suitable as emerging candidates in memory device applications.

1. Introduction

Rare earth manganites with perovskite structure ($RMnO_3$, R = rare earth elements) have obtained extensive attentions ever since its discovery around the 1950s[1] due to their interesting physical phenomena, such as colossal magnetoresistance (CMR) effect, charge ordering (CO), and multiferroic properties.[2–7] Manganite materials possess a hexagonal structure with $P6_3cm$ space group or an orthorhombic structure with Pbnm space group, depending on A-site ionic radius.[8] Manganese oxides with a hexagonal structure represent multiferroic property, having promising applications as sensors and nonvolatile random-access memory (RAM) devices,[9–11] while an orthorhombic structure with magnetic disturbance causes spin-lattice coupling due to the inverse Dzyaloshinskii–Moriya interaction.[9] The well-known example of multiferroic manganite is $YMnO_3$ (YMO) with a hexagonal structure. The tilted MnO_5 blocks cause the displacement of Y^{3+} ions along c-axis, which lead to the ferroelectric polarization in YMO.[12,13] An antiferromagnetic ordering has been observed at Neel temperature ≈74 K with the ferroelectric transition at Curie temperature ≈914 K in this compound.[14–16] The formation of mixed valent manganites can be achieved by doping a divalent at rare-earth (RE) site. Hole doping by Sr^{2+} at Y-sites (crystal structure of $Y_{1-x}Sr_xMnO_3$[17,18] is shown as Figure S1, Supporting Information) can induce Mn^{3+} and Mn^{4+} states, which alter the properties of YMO because of the Zener double exchange.

The treatment of swift heavy ion (SHI) irradiation can be used as a powerful tool to tailor the material properties.[19] Various disorders, such as point or columnar defects, amorphization,

K. N. Rathod, Dr. K. Gadani, Dr. D. Dhruv, H. Boricha, A. Zankat, Dr. P. S. Solanki, Prof. N. A. Shah
Department of Physics
Saurashtra University
Rajkot 360005, India
E-mail: snikesh@yahoo.com, nashah@sauuni.ernet.in

Dr. A. D. Joshi
Department of Nanoscience and Advanced Materials
Saurashtra University
Rajkot 360005, India

Dr. J. P. Singh
Pohang Accelerator Laboratory
Pohang University of Science and Technology
Pohang 37673, South Korea

Dr. K. H. Chae
Advanced Analysis Center
Korea Institute of Science and Technology
Seoul 02792, Republic of Korea

Dr. K. Asokan
Inter University Accelerator Centre
Aruna Asaf Ali Marg, New Delhi 110 067, India

etc. can be observed when SHI pass through the target elements by losing their energy via elastic collisions (nuclear energy loss, S_n) with target nuclei and inelastic collisions (electronic energy loss, S_e) with electrons in the target material. Even, the structural strain modifications in the film can be achieved by SHI irradiation which can tune the various physical properties of the films.[20] There are few reports available in which the resistive switching (RS) properties have been studied with SHI effect. Improvements in the RS by SHI (up to 5×10^{11} ions per cm^2) induced oxygen vacancies in $BiFeO_3$ have been reported by Ravalia et al.[21] Joshi et al. has observed the improved RS in Li:NiO films with SHI irradiation-induced bulk defects or oxygen vacancies at Ag/NiO interface.[22] The same group has observed the oxygen vacancies influenced the RS in Ag^{7+} and Au^{9+} ion-irradiated $La_{0.7}Sr_{0.3}MnO_3$/Ag and Cr:$SrZrO_3$/SRO films, respectively.[23,24] Recent results on RS of ion-irradiated $Y_{1-x}Sr_xMnO_3$ with retention and endurance character indicate stability of memory and resistive window for the device application.[25,26]

Present study reports the modifications of RS property by SHI irradiation on Sr-doped (5%) at yttrium site in nonvolatile YMO thin films. It is well known that the spatial deformation in the structure can firmly affect the RS memory. The doping of divalent strontium (larger) at yttrium (smaller) site in YMO can induce the change in valence states of manganese, which can slightly improve (due to minute concentration of dopant) the double-exchange mechanism, as well as creates the spatial deformation (due to size disorder). Irradiation energy ($\approx$200 MeV) is selected by Monte Carlo simulation in stopping and range of ions in matter (SRIM) code to acquire the most energy irradiated to the films without complete amorphous nature. The consequences of SHI irradiation-induced modifications in the RS behavior have been discussed in the light of oxygen vacancies.

2. Results and Discussions

The Monte Carlo simulation-based calculation was done by SRIM code[27] to simulate the electronic ($S_e \approx 20.26$ keV nm^{-1}) and nuclear ($S_n \approx 0.055$ keV nm^{-1}) energy losses, taken place during the irradiation of $Y_{0.95}Sr_{0.05}MnO_3$ (YSMO) thin films using Ag ions as shown in **Figure 1**a. The ratio S_e/S_n is $\approx 3.7 \times 10^2$ suggests that the role of nuclear energy loss is negligible. As evident from Figure 1a, the maximum electronic loss occurs at the Bragg peak ($\approx$375 MeV). At the Bragg peak, Ag ions move nearly with the Bohr velocity (2.2×10^8 cm s^{-1}) of an electron. Calculated S_e and S_n energy loss with depth are shown in Figure 1b. Estimated energy loss in the first layer (YSMO) is $\approx$2 and $\approx$0.3 MeV for the second layer (SiO_2). Through the first two layers, S_e is dominant over S_n. Ag ions lose their energy completely after $\approx$23.86 µm depth in Si substrate, i.e., range of ions with energy $\approx$197.7 MeV in Si substrate. The range of ions is much higher than the films' thickness ($\approx$100 nm), so projectile Ag ions penetrate deep inside the substrates through films, and ion implantation possibility in the manganite films can be neglected. Moreover, the Ag ions with high energy and high velocity are stopped inside the substrate. Stopping of Ag ions inside the substrate can be realized as the much high thickness of the Si substrate ($\approx$500 µm) than the ion stopping ($\approx$23.86 µm). By selecting aforesaid energy for SHI, it is strongly
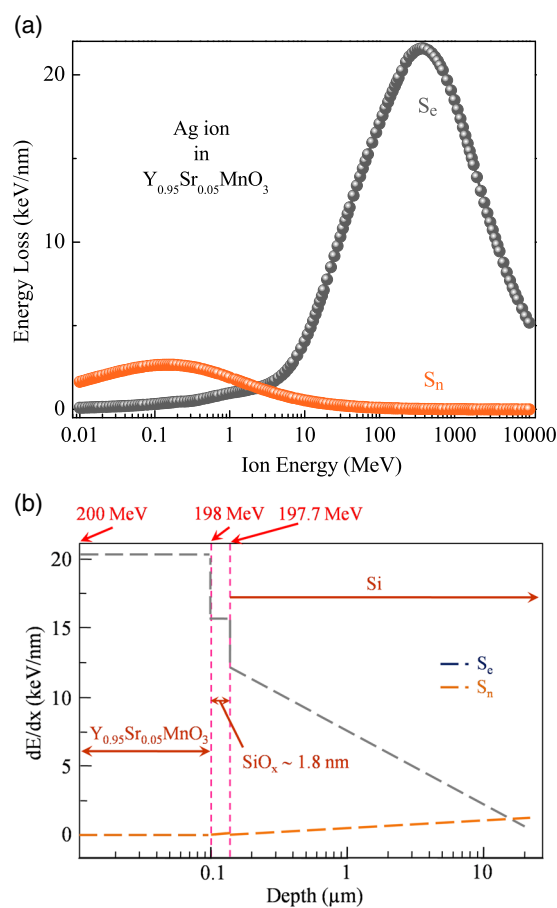
Figure 1. a) Simulated electronic (S_e) and nuclear (S_n) energy loss spectra with ion energy. b) S_e and S_n energy loss as a function of depth calculated using SRIM-2008 for 200 MeV Ag^{15+} ions.

believed that the structure of oxide materials (including manganite thin films) gets modified by the displacement of target atoms through the heavy Ag ions across the lattice. The changes in the structure can be studied by performing X-ray diffraction (XRD) measurements followed by further investigations on the effective structure–property correlations.

The structural investigations by XRD measurements of all the films are shown as the diffraction spectra in **Figure 2**. All the films are oriented in a single direction, exhibiting a hexagonal phase with intense peaks (400) at $\approx$69° along Si substrate peaks (400). It is evident from diffraction patterns that all the films having a single-phase nature with a–axis (h00) growth. The peaks at lower 2θ of YSP and YS1 get vanished in YS2 and YS3 due to the SHI irradiation-induced structural deformation. The intensity of YSMO peaks (400) from YSP to YS3 gets reduced pointing out that crystallization gets modified effectively. The values of 2θ peak (400) positions for all four YSMO films' reflections are listed in **Table 1**. Peak separation between the substrate and the film, increases from YSP to YS2 (indicated by a dotted line in the right panel of Figure 2) indicating an enhanced lattice mismatch or strain with irradiation due to the improved defect environment. This defect environment gets relaxed in YS3 film due to the local annealing effect. The calculated strain using
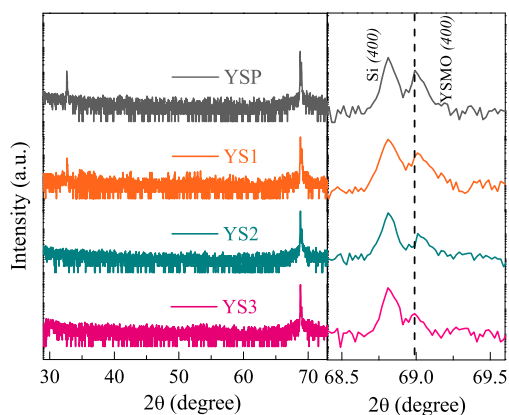
Figure 2. X-ray diffraction patterns in semi-logarithmic scale; right panel: enlarged view of the most intense peaks.

Table 1. Strain, Raman mode position, and RMS roughness.

Sr. no.	Thin film	XRD peak (400) position [°]	Strain [%]	Intense A_1 mode [cm^{-1}]	Raman fit [R^2]	RMS roughness [nm]
1	YSP	68.93	+0.23	662.10	0.906	0.69
2	YS1	68.95	+0.25	657.74	0.863	0.81
3	YS2	68.96	+0.26	657.37	0.910	1.69
4	YS3	68.92	+0.22	661.04	0.903	1.45

formula $\delta\,(\%) = [(d_{\text{substrate}} - d_{\text{film}})/d_{\text{substrate}}] \times 100$, indicating a tensile strain, and is tabulated in Table 1. Increase in tensile strain from YSP to YS2 film and then strain relaxation for YS3 with suppression in peak intensity suggests the crystallinity of the films is highly affected by high energy transferred to the films due to SHI irradiation.

Raman spectra of YSP, YS1, YS2, and YS3 thin films are shown in **Figure 3**. The A_1 Raman active modes are observed in all the thin films. No clear peak shifting has been observed for symmetry at $\approx$300 cm^{-1}, while symmetry at $\approx$433 cm^{-1} (indicated by a down arrow in Figure 3) is not prominent in
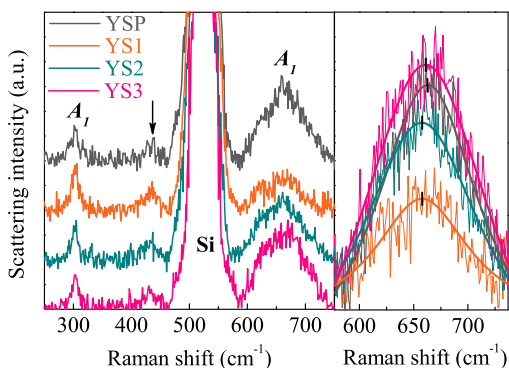

Figure 3. Raman spectra of YSP, YS1, YS2, and YS3 thin films; right panel: baseline-corrected higher frequency A_1 symmetry modes with Lorentzian function fits.

the intensity. Both of these peaks are in agreement to the Raman modes observed by Iliev et al. for hexagonal YMO.[28] The peaks positioned at $\approx$520 cm^{-1} originate from the vibration modes of Si substrates.[29,30] Most intense Raman active modes are at $\approx$660 cm^{-1} which are fitted using a Lorentzian function and is shown in Figure 3 (right panel). The coefficient of determination (COD) R^2 is depicted in Table 1, indicating all the films are well fitted to the Lorentzian function [except YS1 film ($R^2 \approx 0.863$)]. Larger Sr ions doped at smaller Y ions create a large size disorder in the system which leads to the most prominent peaks at $\approx$660 cm^{-1} rather than at $\approx$681 cm^{-1} observed by Iliev et al.[28] and $\approx$685 cm^{-1} by Liu et al.[29] However, the most active Raman modes are in agreement to the calculated longitudinal optic (LO) and transverse optic (TO) modes by Iliev et al.[28] The shift in peak positions toward lower frequencies (i.e., red shift) with irradiation indicating an improved tensile strain[31] following the strain results is discussed in the XRD analysis. Strain relaxation has been observed in YS3 as it shows the peak shifting toward a higher frequency. This red shifting from YSP to YS2 suggests the phonon softening due to increased tensile strain, while YS3 suggests the weakening of the phonon softening due to strain relaxation process.

To understand the changes in surface morphology of pristine and irradiated films, atomic force microscopy (AFM) measurements were performed. Surface modifications with irradiation were studied using WSxM software.[32] Images were initially processed by the flatten filter tool to remove the noises from the films. 2D images (top row) of YSP, YS1, YS2, and YS3 films with 3D images (bottom row) are shown in **Figure 4**. It is observed that YSP film exhibits island-like morphology, whereas irradiated films display hillock-like defects formed due to the irradiation. These defects are increased up to YS2 film and decreased for YS3 film. The size of the defects increases from YS1 to YS2 and decreases for YS3. The density of defects and maximum height follows the same manner. Root-mean-square (RMS) roughnesses of YSP, YS1, YS2, and YS3 have been estimated to be $\approx$0.69, $\approx$0.81, $\approx$1.69, and $\approx$1.45 nm, respectively. The size of the defects and RMS roughness is increased up to YS2 signifying an enhancement in the deformation with irradiation due to a large amount of energy transferred to the films. This deformation gets annealed out and recrystallizes in YS3 film, observed as a smooth surface. Oxygen vacancies (one of the possible defects present on the surface) increase with irradiation due to the charge-transfer processes that annealed out for YS3 film.

Standard Rutherford backscattering spectrometry (RBS) operated with alpha particles ($\approx$2 MeV) can only provide less intense oxygen peak. To overcome this issue and to obtain enhanced oxygen peak, the oxygen resonance mode was undertaken to perform RBS measurement.[33] The difference between two edges of a single peak indicates the energy loss of projectile He ions in the element. From the inset of **Figure 5**a, it is observed that the oxygen content decreases from YSP to YS2 film, signifying increased oxygen vacancies in the films irradiated up to 1×10^{12} ions per cm^2 dose. For YS3 film, the oxygen content increases showing the decrease in oxygen vacancies.

SIMNRA software[34] was used to simulate the obtained RBS spectra. A simulated spectrum of YSP film is shown in the inset of Figure 5b. The simulated spectrum can be used to calculate thickness and chemical composition of the films, as shown in
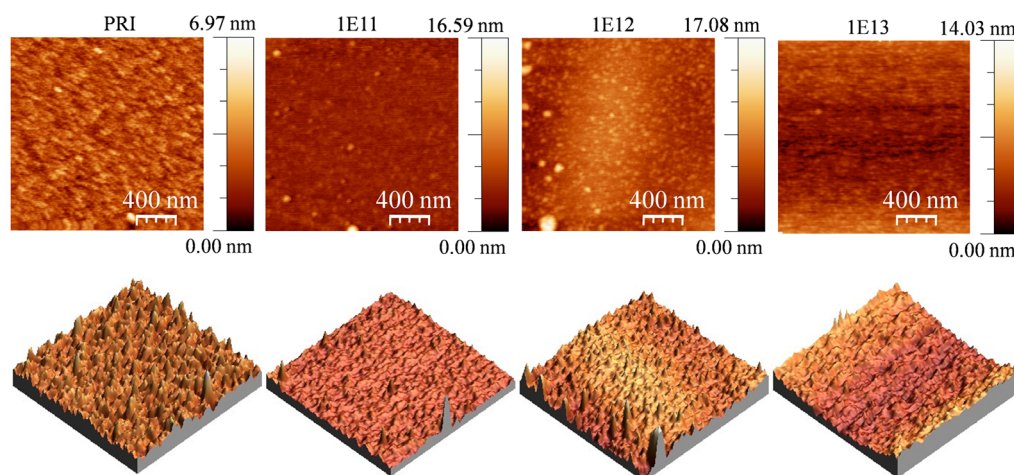
**Figure 4.** 2D AFM images (top) and respective 3D images (bottom).
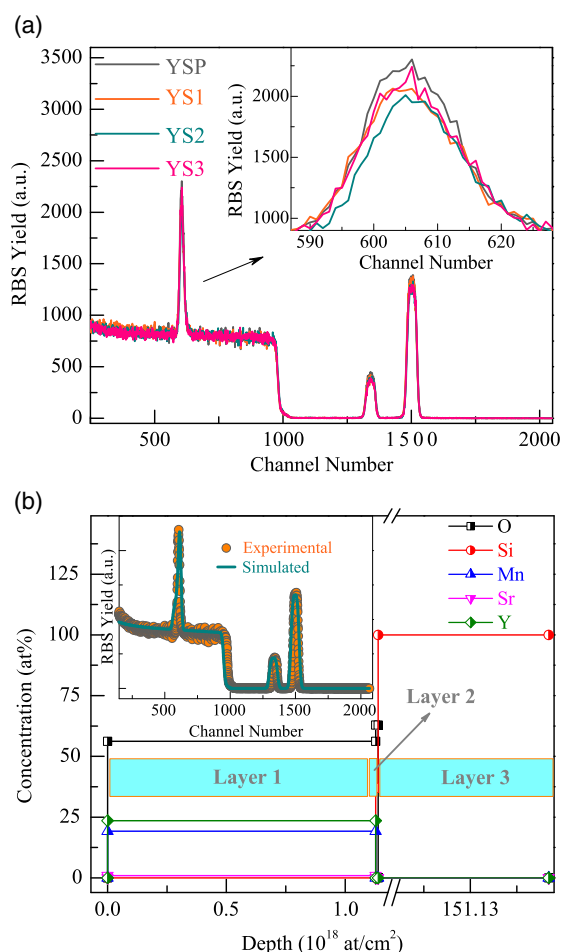
Figure 5. a) Resonance-mode RBS spectra of all thin films; inset: enlarged view of oxygen peak. b) The elemental depth profile of YSP film derived from SIMNRA-simulated spectrum; inset: SIMNRA-simulated spectrum of YSP thin film.

depth profile (Figure 5b) for YSP film (layer 1–YSMO film and layer 3–Si substrate). We have considered SiO_x layer as a layer 2 during the simulation for all RBS spectra. The thickness of SiO_x layer is found to be ≈1.8 nm for YSP film. YSP film thickness is ≈98.2 nm, close to the thickness ≈100 nm measured by profilometer. Depth profile confirms the presence of oxygen vacancies in YSP film. From the simulation performed for all the films, estimated oxygen vacancy concentrations are $\approx6.28\%$ (YSP), $\approx9.77\%$ (YS1), $\approx11\%$ (YS2), and $\approx3.05\%$ (YS3). The values of oxygen content (x) in SiO_x layer for YSP, YS1, YS2, and YS3 films are estimated to be $\approx1.8776(5)$, $\approx1.8328(4)$, $\approx1.8179(4)$, and $\approx1.8447(7)$, respectively. Variation in oxygen content with irradiation fluence has been observed in SiO_x layer. The energy required to remove oxygen from SiO_x is very small,[35] so it is expected that the removal of oxygen from SiO_x is present with the diffusion process. Diffusion of oxygen from SiO_x layer to the film results into oxygen vacancy improvement in SiO_x region up to YS2 film, whereas the annealing of defects reduces the loss of oxygen for SiO_x layer in YS3 film. It is interesting to highlight that the oxygen loss becomes effective from YSP to YS2 film, whereas the highest fluence-based film (i.e., YS3) possesses the minimum oxygen loss effect which can be understood as: when the ion irradiation was performed for YS1 and YS2 irradiated films, it introduces a large amount of heat/energy inside the lattice of the films as well as at SiO_x layers between the substrate and film. As a consequence, a large number of defects get generated (as discussed in AFM analysis). Upon increase in ion fluence (above YS2), the energy dispersed within the lattice crosses the threshold energy level (due to prolonged time used for irradiation)[21] that provides local heating effect or annealing effect inside the lattice of YS3 film. As a result, this effect encourages recrystallization in the film (supported by reduced strain effect from the XRD analysis) that efficiently reduces the defect density (including oxygen vacancies) in the lattice of YS3 film.

To understand the modifications in local electronic structures of Mn ions due to the SHI irradiation, we performed near-edge
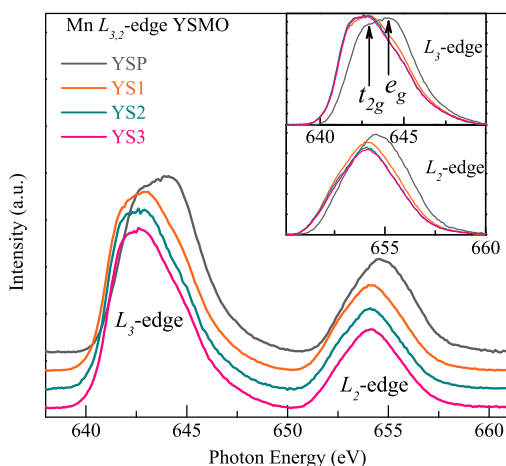
Figure 6. Normalized NEXAFS spectra at Mn $L_{3,2}$-edge; inset: enlarged view of baseline-corrected L_3- and L_2-edges.

X-ray absorption fine structure (NEXAFS). The normalized NEXAFS spectra of Mn $L_{3,2}$-edge of YSP, YS1, YS2, and YS3 films are shown in **Figure 6**. These spectra resulted due to the electronic transitions from 2p to 3d states and are separated into two regions, L_2 and L_3 due to spin-orbit splitting and provide information about the density of unoccupied Mn 3d states.[36] The hole doping by Sr evolves the configuration change from $t_{2g}^3 e_g^1$ (Mn^{3+}) of YMO to $t_{2g}^3 e_g^0$ (Mn^{4+}) of YSMO, which creates mixed valence nature in Mn ions primarily the Mn^{3+} and Mn^{4+} states. The intensity of L_3-edge is doubled as compared with L_2-edge due to the degeneracy. The L_3-edge is more susceptible to the local environment as compared with L_2-edge, due to which the spectral shift is ≈ 1.5 eV for L_3-edge and ≈ 0.5 eV for L_2-edge for all the films (inset of Figure 6).[37] Decrease in 3d orbital count causes the change in electrostatic energy which forces the chemical shifting of peaks toward higher photon energy.[38] As compared with the pristine, the L_3- and L_2-edges of the irradiated films shift toward lower photon energy. This result signifies more spectral weight of Mn^{3+} than that of Mn^{4+}[39,40] which can be due to tensile strain-induced modifications in the irradiated films.[41] The creation of more oxygen vacancies is attributed to the reduction in Mn valence state (Mn^{4+} to Mn^{3+}), shift the L-edges to lower energy.[42–47]

As presented in **Figure 7**, the deconvoluted L_3- and L_2-edges split into t_{2g} and e_g orbitals due to the crystal field effects. The statistical measures (R^2) or COD are ≈ 0.996 for almost all films signifying better fitting. The separation between t_{2g} and e_g orbitals (crystal field splitting) increases from YSP (≈ 1.60 eV) to YS3 (≈ 1.66 eV) film. This slight variation in the peak separation is attributed to the modifications in the energy band structure of the YSMO films caused by irradiation-induced defects.[21] Higher intensity has been observed for e_g than that of t_{2g} for all the films because Sr^{2+} doping in YMO creates four vacant/unoccupied states in e_g, whereas three vacant/unoccupied states in t_{2g}.[48–50] The intensity of t_{2g} peak gets improved while e_g peak intensity reduces with irradiation, implying an increase in Mn^{3+} ions due to increased oxygen vacancy formation.[42] High-energy irradiation leads to the transformation of Mn^{4+} to Mn^{3+} states. This can be understood as, reduction of two Mn^{4+} to
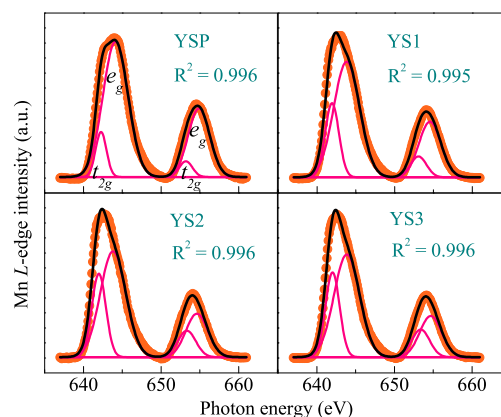

Figure 7. Deconvoluted t_{2g} and e_g peaks of L_3- and L_2-edges.

Mn^{3+} by two electrons offered by V_o^{2+}, similar to Mn^{3+}–Mn^{2+} transition given by Griffin et al.[51]

$$2Mn^{4+} + O_o^{2-} \rightarrow 2Mn^{3+} + \frac{1}{2}O_2 \text{ (gas)} + V_o^{2+} \qquad (1)$$
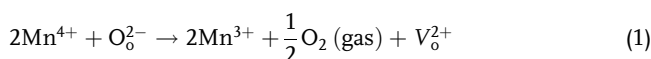
The presence of oxygen vacancy results in pronounced RS in a manganite-based thin films and devices.[47,52] Because Ag is an electrochemically active metal,[53,54] the redox process and diffusion of Ag electrode can lead to conducting filamentary paths[55] that contribute to RS. However, the dimensions of the electrodes were kept almost the same (electrodes prepared after irradiation, so, one can expect similar effects of electrodes in all the films) and provided ohmic contact (mentioned in the Experimental Section) at the top electrode (Ag and YSMO contact) indicates no RS.[56] For the bottom electrode (Ag through SiO$_2$ contact), Ag ions diffuse through native SiO$_2$ layer to the Si substrate due to the narrow thickness ≈ 1.8 nm of SiO$_2$ layer. The metal (Ag) and semiconductor (Si) forms Schottky contact at the bottom electrode. All the electrodes were prepared after irradiation. So, it is expected that irradiation is responsible for the RS effect, and not the Schottky effect. In this context, a local switching phenomenon associated with the electrode diffusion can be negligible over other dominating ones. Another possibility of switching arises from the redox reaction of native SiO$_x$ layer and oxygen vacancies present in the films. The RS mechanism for perovskite manganite thin films shows rupture and formation of Mn^{3+}–O^{2-}–Mn^{4+} string induced by the migration of oxygen ions or vacancies in the MnO lattice.[57–59]

RS phenomenon, as shown in **Figure 8**, was studied by cyclic I–V characteristics of YSMO pristine and irradiated films grown on Si substrates using the direct voltage sweeping mode. The YSMO/Si device with two-probe technique is schematically shown as the inset of Figure 8, in which Ag electrodes have been used as metal contacts and an interface is shown as a native SiO$_x$ layer. The dc bias voltage sweeping sequences (as numbers) and directions (as arrows) are shown in Figure 8. Observed rectifying I–V characteristics are similar to p–n junction diode. Lower current in reverse bias as compared with forward bias, indicates an increase in barrier height at the interface. The device exhibits bipolar RS followed by an eight-curve wise manner of direction.
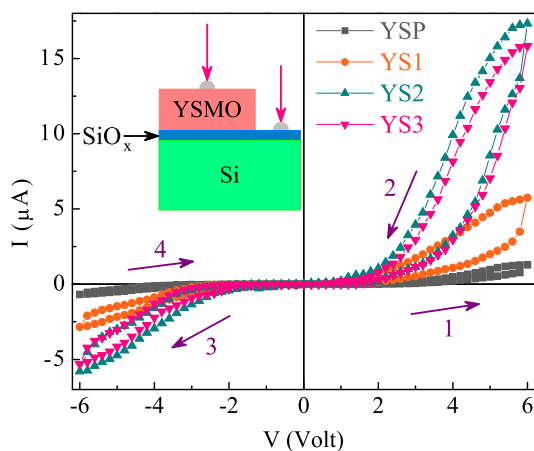
Figure 8. Current–voltage (*I–V*) curves of YSMO/Si films in 0 to ± 6 V.

**Figure 9.** Current–voltage (*I–V*) curves in semi-logarithmic scale.

Current increases as the positive bias is applied during cycle 1 (C1), demonstrating a sharp change at ≈ 5.9 V in the current flow across the interface which shows a SET operation, wherein the device turns into ON state. Device formed perturbed path before the SET operation, wherein electrons have to jump with more energy as compared with the state after SET operation where electrons need less energy. Current followed a different path while reducing positive bias [cycle 2 (C2)], pointing out the clear hysteresis as observed for all the thin films. During C2, current is large as compared with C1 indicating the transformation to low-resistance state (LRS) from high-resistance state (HRS). Cycle 3 (C3) and cycle 4 (C4) are performed in the negative bias. The device retains LRS state in C3, at which the electrons move on the perturbed path. During C4, the device switches to HRS termed as RESET operation, where conducting path formed by oxygen vacancies gets ruptured.

From the Figure 8, enhanced current has been observed from YSP to YS2 which suppresses in YS3 thin film. An increase in oxygen vacancies enhances the exchange mechanism between manganese and oxygen ions, leads to the improved conduction (up to YS2). Reduction in conduction is evident for YS3 film because of decrement in the number of oxygen vacancies. This variation of oxygen vacancies is supported by RBS and NEXAFS measurements. Tensile strain and irradiation-induced defects can be correlated to AFM and Raman measurements which indirectly support the formation of oxygen vacancies. Meanwhile, increased oxygen vacancies of SiO$_x$ layer from YSP to YS2 films (RBS results) also promote RS. These vacancies get annealed out for YS3 film, demonstrating suppression in RS (*I–V* hysteresis) effect. Semi-logarithmic plot is shown in **Figure 9**. RS ratio (R_{HRS}/R_{LRS}) % has been calculated at +3 V (i.e., reading voltage) to analyze the RS behavior quantitatively, and it is estimated to be $\approx 350\%$ for YS2 film. The RS ratio is also found to be increased with irradiation and gets decreased for YS3 film. It is evident from the RS ratio that the RS is highly dependent on ion irradiation. This deviation of the RS ratio with irradiation implies that RS gets improved with irradiation due to the defects mediated conducting path formation. The RS ratio gets suppressed at YS3 due to the annihilation of defects as discussed in AFM analysis.
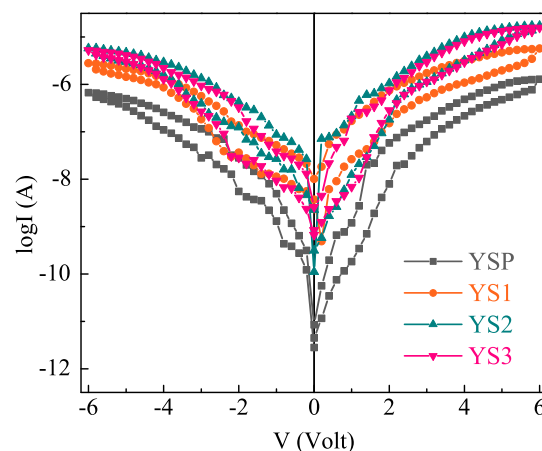
To understand the role of oxygen vacancies and SHI irradiation-induced structural defect modifications in the RS behavior of YSMO films, a physical model (based on spectroscopic results) has been proposed as shown in **Figure 10**. When the high electronic excitations are transferred to the film, energy loss occurs in the form of defects formation. Defects can be as point defects (vacancy, interstitial, etc.) or large density defects (ion track). As a consequence of SHI irradiation, the variation in oxygen vacancies is expected as discussed in the analysis of spectroscopic measurement results. Oxygen vacancies and structural defects increase with more number of free electrons up to YS2 (film and SiO$_x$ layer) that get reduced in YS3 with the local annealing of defects (AFM analysis). The number of electrons is increased for SHI-irradiated films because Mn^{3+} content increases at the expense of Mn^{4+} as discussed in NEXAFS results. Another possibility is that the oxygen loses electrons and forms oxygen vacancies. Moreover, modification in the SiO$_x$ layer is expected with irradiation due to the variation in oxygen content as discussed in RBS analysis. Irradiation-induced oxygen vacancies and structural defects play a vital role to improve the conduction and the RS properties of irradiated films. These oxygen vacancies and structural defects provide conducting
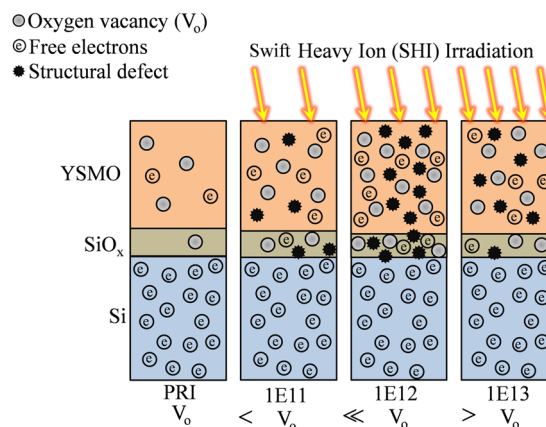
Figure 10. Schematic diagram representing oxygen vacancy and structural defect variations with SHI irradiation.

paths that can easily switch the device from one resistance state to another, can be seen in Figure 8 as better RS for irradiated films.

To understand the migration of oxygen vacancies in the present RS mechanism, we have proposed a dynamic model as shown in **Figure 11**. When there is no bias, oxygen vacancies are randomly distributed in YSMO and SiO_x layer. An electrochemical migration of oxygen vacancies is expected when bias voltage is applied. Positive bias is applied to YSMO film during C1, forces migration of oxygen vacancies to the bottom electrode. The oxygen ions present in SiO_x layer can shift to the film region which creates oxygen vacancies at SiO_x layer. Some oxygen ions support oxygen vacancy annihilation process via the recombination with oxygen vacancies present in YSMO while some get diffused to the top electrode. This diffusion suggests a reduction of SiO_x layer, which decreases the thickness of SiO_x layer. Meanwhile, electrons with high energy can hop from one oxygen vacancy to the adjacent one with an increase in positive bias and move toward the top electrode. During C2, the application of voltage is reducing in the same direction as in C1. Oxygen vacancies (which migrate to the bottom electrode) create a certain path that turns the device into LRS state. Oxygen vacancies of this path act as conducting filaments. SiO_x layer gets reduced as some oxygen ions (of SiO_x layer) further diffused to the top electrode. Here, the oxygen recombination process is also present, but dominated by the conducting filament formed by a large number of oxygen vacancies. The direction of bias is reversed at C3, which changes the direction of oxygen vacancy migration. Oxygen vacancies move to the top electrode whereas oxygen ions travel from the top electrode to the bottom electrode. Oxygen ions (from YSMO and top electrode) recombine with oxygen vacancies in SiO_x layer that can oxidize the SiO_x layer and increase the thickness of SiO_x layer. This event suppresses the current value in reverse bias. The motion of electrons to the bottom electrode with diminutive disturbance is expected as some energy is still enough for electrons to hop at adjacent oxygen vacancies.
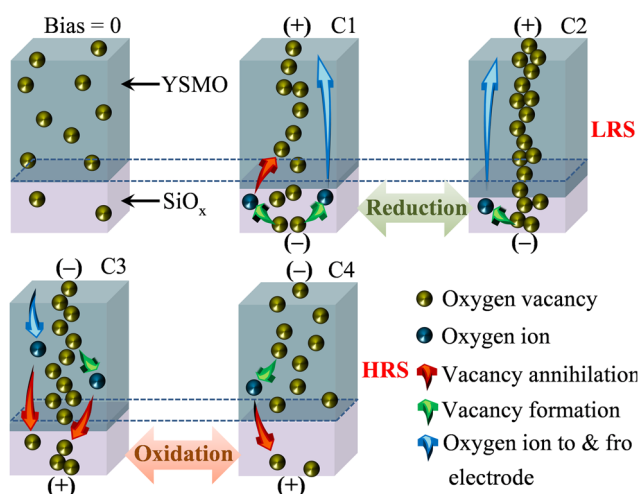
More number of oxygen vacancies gets recombined by oxygen ions in SiO_x layer during C4, which lead to a barrier height increment. Meanwhile, electrons can be trapped by oxygen vacancies with high-energy requirements to hop. The conducting path formed by oxygen vacancies further gets disturbed and ruptures, which can change the device state from LRS to HRS. Throughout the performance of cycles, the variation in SiO_x layer by oxidation and reduction processes plays a vital role in RS characteristics. However, the thickness of a native SiO_x layer is very small, it is expected that the interplay of oxygen vacancies between film and SiO_x layer is controlled through SiO_x layer itself. RS induced by the conducting filamentary path suggests the localized region switching, rather than uniformly distributed throughout the bulk region.

Aforementioned results suggest that SHI irradiation can be used as a tool to improve the RS properties of mixed-valent manganite-based thin film devices. SHI-irradiated manganites are potentially suitable for RRAM devices. Reliability factors, such as retention and endurance are important for RRAM device applications. YMO is a nonvolatile material, but to check the nonvolatile nature of Sr-doped YMO and the SHI effect, further study on retention performance measurement is required. To check the stability/reproducibility of the devices under study, further study on endurance measurement is needed.

3. Conclusions

In summary, we prepared YSMO/Si thin films by pulsed laser deposition (PLD) technique which we used for SHI irradiation. The XRD results reveal the hexagonal phase of thin films oriented in (400) direction with Si substrate. Tensile strain is enhanced with irradiation, because irradiation induces deformations that get relaxed for YS3 film with the annihilation of defects. AFM images show enlarged RMS roughness and defect size with irradiation as an indication of high-energy transfer to the surface of the films. The RBS analysis suggests that oxygen content has been affected by SHI irradiation, showing an oxygen content reduction up to YS2 which gets increased for YS3. Increment in tensile strain (up to YS2) film has been revealed by Raman spectra. NEXAFS investigations confirm the presence of a more number of oxygen vacancies in irradiated films as compared with pristine film, which reduces for YS3 film. RS is improved by SHI irradiation and is controlled by the variation in native SiO_x layer thickness with applied bias. This discussion signifies the importance of YSMO/Si thin film devices for suitable device applications as RRAM.

4. Experimental Section

Solid-state reaction method was used to prepare the targets of $Y_{0.95}Sr_{0.05}MnO_3$ (YSMO) and thin films were fabricated by PLD technique. Precursor materials were initially preheated at 500 °C for 6 h. Starting precursors, such as Y_2O_3, MnO_2, and $SrCO_3$ were mixed thoroughly in proper stoichiometry. After mixing, the material was ground for 6 h and calcined at 950 °C for 24 h followed by grinding and pelletizing. Pellets were sintered at 1100 °C for 48 h and used as targets. Thin films were deposited on n-type single-crystalline Si (100) substrate using PLD technique. Low pressure of 100 mTorr was maintained for oxygen vacancy formation. The KrF excimer laser was used to ablate the targets with ≈1.8 J cm^{-2} energy

Figure 11. Schematic illustration of a model representing a possible RS mechanism with oxygen vacancy migration (C1: cycle 1 from 0 to +6 V, C2: cycle 2 from +6 to 0 V, C3: cycle 3 from 0 to −6 V, and C4: cycle 4 from −6 to 0 V).

density/laser fluence and 10 Hz frequency. Substrate temperature was kept $\approx 700\,^\circ C$ with the substrate-to-target distance $\approx 50\,mm$. The PLD-grown thin films were irradiated by Ag^{15+} ions of 200 MeV energy using 15 UD Pelletron accelerator available at IUAC, New Delhi. The pristine, 1×10^{11} ions per cm^2, 1×10^{12} ions per cm^2, and 1×10^{13} ions per cm^2 irradiated thin films are denoted as YSP, YS1, YS2, and YS3, respectively. Thickness of the thin films was confirmed to be $\approx 100\,nm$ as measured by thickness profilometer. The crystallinity and morphology of the films were studied by XRD using the Cu Kα source of Philips diffractometer (PW 3040/60, X'pert PRO) and AFM using Digital Instruments, Nanoscope IIIa, atomic force microscope in the tapping mode. All thin films were characterized by RBS at 5SDH–1.7 MV Tandem accelerator, PARAS (Pelletron Accelerator for RBS–AMS System), IUAC, New Delhi to verify the change in elemental compositions, followed by Raman spectroscopy using Renishaw inVia Raman microscope in backscattering geometry to identify the deformation. Near-–edge X-ray absorption fine structure (NEXAFS) measurements were carried out to confirm the change in the oxidation state of Mn using 10D XAS KIST beam line of Pohang Light Source (PLS), Korea. To study the effect of irradiation on RS properties of thin films, hysteretic current–voltage (I–V) measurements were performed by sweeping the dc bias voltage from $0\,V \rightarrow +6\,V \rightarrow 0\,V \rightarrow -6\,V \rightarrow 0\,V$ using Keithley 6517B electrometer. For I–V measurements, silver contacts (of the size $1 \times 1\,mm^2$) were used to provide the ohmic contact with transition metal oxides[60] at the top electrode and Schottky contact at the bottom electrode. To study the transport across thin film and substrate, current perpendicular to plane (CPP) geometry was used.

Supporting Information

Supporting Information is available from the Wiley Online Library or from the author.

Conflict of Interest

The authors declare no conflict of interest.

[1] D. G. Tomuta, S. Ramakrishnan, G. J. Nieuwenhuys, J. A. Mydosh, *J. Phys.: Condens. Matter* **2001**, *13*, 4543.

[2] C. N. R. Rao, B. Raveau, *Colossal Magnetoresistance, Charge Ordering and Related Properties of Manganese Oxides*, World Scientific, Singapore **1998**.

[3] Y. Tokura, Y. Tomioka, H. Kuwahara, A. Asamitsu, Y. Moritomo, M. Kasai, *J. Appl. Phys.* **1996**, *79*, 5288.

[4] H. Y. Hwang, S. W. Cheong, P. G. Radaelli, M. Marezio, B. Batlogg, *Phys. Rev. Lett.* **1995**, *75*, 914.

[5] R. V. Helmolt, J. Wecker, B. Holzapfel, L. Schultz, K. Samwer, *Phys. Rev. Lett.* **1993**, *71*, 2331.

[6] Z. J. Huang, Y. Cao, Y. Y. Sun, Y. Y. Xue, C. W. Chu, *Phys. Rev. B* **1997**, *56*, 2623.

[7] T. Kimura, T. Goto, H. Shintani, K. Ishizaka, T. Arima, Y. Tokura, *Nature* **2003**, *426*, 55.

[8] Y. H. Huang, H. Fjellvag, M. Karpinnen, B. C. Hauback, H. Yamauchi, J. B. Goodenough, *Chem. Mater.* **2006**, *18*, 2130.

[9] S. W. Cheong, M. Mostovoy, *Nat. Mater.* **2007**, *6*, 13.

[10] N. Fujimura, T. Ishida, T. Yoshimura, T. Ito, *Appl. Phys. Lett.* **1996**, *69*, 1011.

[11] R. Ramesh, N. A. Spaldin, *Nat. Mater.* **2007**, *6*, 21.

[12] B. B. V. Aken, T. T. M. Palstra, A. Filippetti, N. A. Spaldin, *Nat. Mater.* **2004**, *3*, 164.

[13] S. Lee, A. Pirogov, J. H. Han, J. G. Park, A. Hoshikawa, T. Kamiyama, *Phys. Rev. B* **2005**, *71*, 180413.

[14] D. Y. Cho, J. Y. Kim, B. G. Park, K. J. Rho, J. H. Park, H. J. Noh, B. J. Kim, S. J. Oh, H. M. Park, J. S. Ahn, H. Ishibashi, S. W. Cheong, J. H. Lee, P. Murugavel, T. W. Noh, A. Tanaka, T. Jo, *Phys. Rev. Lett.* **2007**, *98*, 217601.

[15] T. Katsufuji, S. Mori, M. Masaki, Y. Moritomo, N. Yamamoto, H. Takagi, *Phys. Rev. B* **2001**, *64*, 104419.

[16] C. C. Neacsu, B. B. V. Aken, M. Fiebig, M. B. Raschke, *Phys. Rev. B* **2009**, *79*, 100107.

[17] A. S. Gibbs, K. S. Knight, P. Lightfoot, *Phys. Rev. B* **2011**, *83*, 094111.

[18] S. K. Abbas, S. Atiq, S. Riaz, S. M. Ramay, S. Naseem, *Mater. Chem. Phys.* **2017**, *200*, 128.

[19] B. Angadi, Y. S. Jung, W. K. Choi, R. Kumar, K. Jeong, S. W. Shin, J. H. Lee, J. H. Song, M. W. Khan, J. P. Srivastava, *Appl. Phys. Lett.* **2006**, *88*, 142502.

[20] S. B. Ogale, Y. H. Li, M. Rajeswari, L. S. Riba, R. Ramesh, T. Venkatesan, A. J. Mills, R. Kumar, G. K. Mehta, R. Bathe, S. I. Patil, *J. Appl. Phys.* **2000**, *87*, 4210.

[21] A. Ravalia, M. Vagadia, P. S. Solanki, S. Gautam, K. H. Chae, K. Asokan, N. A. Shah, D. G. Kuberkar, *J. Appl. Phys.* **2014**, *116*, 153701.

[22] U. S. Joshi, S. J. Trivedi, K. H. Bhavsar, U. N. Trivedi, S. A. Khan, D. K. Avasthi, *J. Appl. Phys.* **2009**, *105*, 073704.

[23] K. H. Bhavsar, U. S. Joshi, *Nucl. Instrum. Methods Phys. Res. B* **2016**, *379*, 95.

[24] K. H. Bhavsar, U. S. Joshi, B. V. Mistry, S. A. Khan, D. K. Avasthi, *Radiat. Eff. Defects Solids* **2011**, *166*, 718.

[25] K. Gadani, K. N. Rathod, D. Dhruv, H. Boricha, K. Sagapariya, A. D. Joshi, D. D. Pandya, K. Asokan, P. S. Solanki, N. A. Shah, *J. Alloys Compd.* **2019**, *788*, 819.

[26] B. Hirpara, K. Gadani, K. Sagapariya, H. Gohil, D. Sanghvi, A. D. Joshi, K. Asokan, P. S. Solanki, N. A. Shah, *Thin Solid Films* **2019**, *685*, 151.

[27] J. P. Biersack, L. G. Haggmark, *Nucl. Instrum. Methods Phys. Res. B* **1980**, *174*, 257.

[28] M. N. Iliev, H. G. Lee, V. N. Popov, M. V. Abrashev, A. Hamed, R. L. Meng, C. W. Chu, *Phys. Rev. B* **1997**, *56*, 2488.

[29] L. Y. Feng, W. Bei, Z. H. Wu, L. X. Yang, G. Y. Zong, Z. W. Feng, *Chin. Phys. Lett.* **2010**, *27*, 056801.

[30] I. Iliescu, M. Boudard, O. C. Pluchery, L. Rapenne, H. Roussel, *J. Solid State Chem.* **2014**, *220*, 245.

[31] M. Huang, H. Yan, C. Chen, D. Song, T. F. Heinz, J. Hone, *Proc. Natl. Acad. Sci. USA* **2009**, *106*, 7304.

[32] I. Horcas, R. Fernandez, J. M. Gomez–Rodriguez, J. Colchero, J. Gomez–Herrero, A. M. Baro, *Rev. Sci. Instrum.* **2007**, *78*, 013705.

[33] P. Mohanty, V. P. Singh, N. C. Mishra, S. Ojha, D. Kanjilal, C. Rath, *J. Phys. D: Appl. Phys.* **2014**, *47*, 315001.

[34] M. Mayer, *Nucl. Instrum. Methods Phys. Res. B* **2014**, *332*, 176.

[35] G. Roma, Y. Limoge, *Phys. Rev. B* **2004**, *70*, 174101.

[36] K. Asokan, Y. S. Chen, C. W. Pao, H. M. Tsai, C. W. O. Lee, C. H. Lin, H. C. Hsueh, D. C. Ling, W. F. Pong, J. W. Chiou, M. H. Tsai, O. Pena, C. Moure, *Appl. Phys. Lett.* **2009**, *95*, 131901.

[37] D. K. Shukla, R. Kumar, S. Mollah, R. J. Choudhary, P. Thakur, S. K. Sharma, N. B. Brookes, M. Knobel, *J. Appl. Phys.* **2010**, *107*, 09D903.

[38] M. Abbate, F. M. F. de Groot, J. C. Fuggle, A. Fujimori, O. Strebel, F. Lopez, M. Domke, G. Kaindl, G. A. Sawatzky, M. Takano, Y. Takeda, H. Eisaki, S. Uchida, *Phys. Rev. B* **1992**, *46*, 4511.

[39] R. Qiao, T. Chin, S. J. Harris, S. Yan, W. Yang, *Curr. Appl. Phys.* **2013**, *13*, 544.

[40] M. Varela, M. P. Oxley, W. Luo, J. Tao, M. Watanabe, A. R. Lupini, S. T. Pantelides, S. J. Pennycook, *Phys. Rev. B* **2009**, *79*, 085117.

[41] R. U. Chandrasena, W. Yang, Q. Lei, M. U. D. Jaime, K. D. Wijesekara, M. Golalikhani, B. A. Davidson, E. Arenholz, K. Kobayashi, M. Kobata, F. M. F. de Groot, U. Aschauer, N. A. Spaldin, X. Xi, A. X. Gray, *Nano Lett.* **2017**, *17*, 794.

[42] H. Guo, J. Wang, X. He, Z. Yang, Q. Zhang, K. Jin, C. Ge, R. Zhao, L. Gu, Y. Feng, W. Zhou, X. Li, Q. Wan, M. He, C. Hong, Z. Guo, C. Wang, H. Lu, K. Ibrahim, S. Meng, H. Yang, G. Yang, *Adv. Mater. Interfaces* **2016**, *3*, 1500753.

[43] C. Wang, K. Jin, L. Gu, H. Lu, S. Li, W. Zhou, R. Zhao, H. Guo, M. He, G. Yang, *Appl. Phys. Lett.* **2013**, *102*, 252401.

[44] Z. Li, M. Bosman, Z. Yang, P. Ren, L. Wang, L. Cao, X. Yu, C. Ke, M. B. H. Breese, A. Rusydi, W. Zhu, Z. Dong, Y. L. Foo, *Adv. Funct. Mater.* **2012**, *22*, 4312.

[45] M. Nord, P. E. Vullum, M. Moreau, J. E. Boschker, S. M. Selbach, R. Holmestad, T. Tybell, *Appl. Phys. Lett.* **2015**, *106*, 041604.

[46] R. Zhao, K. Jin, Z. Xu, H. Guo, L. Wang, C. Ge, H. Lu, G. Yang, *Appl. Phys. Lett.* **2013**, *102*, 122402.

[47] S. G. Choi, H. Lee, H. Choi, S. Chung, H. Park, *J. Phys. D: Appl. Phys.* **2011**, *44*, 422001.

[48] K. Asokan, J. C. Jan, K. V. R. Rao, J. W. Chiou, H. M. Tsai, S. Mookerjee, W. F. Pong, M. H. Tsai, R. Kumar, S. Husain, J. P. Srivastava, *J. Phys.: Condens. Matter* **2004**, *16*, 3791.

[49] G. Anjum, R. Kumar, S. Mollah, P. Thakur, S. Gautam, K. H. Chae, *J. Phys. D: Appl. Phys.* **2011**, *44*, 075403.

[50] K. Asokan, H. M. Tsai, C. W. Bao, J. W. Chiou, W. F. Pong, G. Sonia, T. J. S. Anand, *Spectrochim. Acta, Part A* **2008**, *70*, 454.

[51] S. M. Griffin, M. Reidulff, S. M. Selbach, N. A. Spaldin, *Chem. Mater.* **2017**, *29*, 2425.

[52] Z. Xu, K. Jin, L. Gu, Y. Jin, C. Ge, C. Wang, H. Guo, H. Lu, R. Zhao, G. Yang, *Small* **2012**, *8*, 1279.

[53] D. Liu, H. Cheng, X. Zhu, G. Wang, N. Wang, *ACS Appl. Mater. Interfaces* **2013**, *5*, 11258.

[54] F. Pan, C. Chen, Z. Wang, Y. Yang, J. Yang, F. Zeng, *Prog. Nat. Sci.: Mater. Int.* **2010**, *20*, 01.

[55] I. Valov, *Semicond. Sci. Technol.* **2017**, *32*, 093006.

[56] X. G. Chen, X. B. Ma, Y. B. Yang, L. P. Chen, G. C. Xiong, G. J. Lian, Y. C. Yang, J. B. Yang, *Appl. Phys. Lett.* **2011**, *98*, 122102.

[57] Y. B. Nian, J. Strozier, N. J. Wu, X. Chen, A. Ignatiev, *Phys. Rev. Lett.* **2007**, *98*, 146403.

[58] D. S. Kim, Y. H. Kim, C. E. Lee, Y. T. Kim, *Phys. Rev. B* **2006**, *74*, 174430.

[59] X. Chen, N. Wu, J. Strozier, A. Ignatiev, *Appl. Phys. Lett.* **2006**, *89*, 063507.

[60] S. J. Ikhmayies, N. M. A. El-Haija, R. N. Ahmad-Bitar, *J. Semicond.* **2015**, *36*, 033005.